

# Vortex Patches under Cnoidal Waves

Christopher W. Curtis  
Henrik Kalisch

## Introduction

### Model

Throughout, we are attempting to describe the simultaneous evolution of a free surface  $y = \eta(x, t) + H$ , and a compactly supported patch of vorticity  $\omega(x, y, t)$  underneath the free surface. We suppose along the curve  $z = 0$  that we have a solid boundary so that the normal velocity is identically zero. In an inviscid, incompressible fluid, we can represent the fluid velocity  $\mathbf{u}(x, y, t)$  generated by a vortex patch characterized by vorticity profile  $\omega(\mathbf{x}, t)$ ,  $\mathbf{x} = (x, y)$ , over the compact domain  $\Omega(t)$  via the integral equation

$$\mathbf{u}(\mathbf{x}, t) = \int_{\Omega(t)} \mathbf{K}(\mathbf{x} - \tilde{\mathbf{x}}) \omega(\tilde{\mathbf{x}}, t) d\tilde{\mathbf{x}} + \nabla \tilde{\phi}, \quad \Delta \tilde{\phi} = 0.$$

where  $\omega$  is the vorticity, and  $\mathbf{K}$  is the standard Biot-Savart kernel. The harmonic function  $\tilde{\phi}$  is used to address boundary conditions as explained in [1]. An attractive means for discretizing this equation as summarized in [2] is to approximate the vorticity  $\omega$  via the expression  $\omega_d$  which is given by a collection of  $N$  point-vortices at positions  $\mathbf{x}_j(t)$  via the expansion

$$\omega_d(\tilde{\mathbf{x}}, t) = \sum_{j=1}^N \frac{\Gamma_j}{\delta^2} \chi\left(\frac{\tilde{\mathbf{x}} - \mathbf{x}_j(t)}{\delta}\right), \quad \mathbf{x}_j(t) = (x_j(t), y_j(t)), \quad (1)$$

where  $\chi$  is some appropriately chosen mollifier, see [3], and  $\Gamma_j$  is the circulation associated with the point vortex at  $\mathbf{x}_j(t)$ . This discretization is an example of a Particle-Vortex Method (PVM). Thus, we can reduce the problem of tracking the evolution of the vortex patch to describing the motion of the point vortices via the system of ODE's

$$\frac{d\mathbf{x}_j}{dt} = \sum_{l \neq j}^N \Gamma_l \mathbf{K}_\delta(\mathbf{x}_j - \mathbf{x}_l) + \nabla \tilde{\phi}(\mathbf{x}_j, t), \quad \mathbf{K}_\delta(\mathbf{x}) = \frac{1}{\delta^2} \int_{\mathbb{R}^2} \mathbf{K}(\mathbf{x} - \tilde{\mathbf{x}}) \chi\left(\frac{\tilde{\mathbf{x}}}{\delta}\right) d\tilde{\mathbf{x}}.$$

Choosing, as in [3], the mollifier  $\chi$  to be the fourth-order kernel

$$\chi(r) = 2e^{-r^2} - \frac{1}{2}e^{-r^2/2},$$

introducing periodic boundary conditions in the lateral direction and enforcing the presence of a solid boundary along the curve  $z = 0$  then modifies the above dynamical system to be

$$i \frac{dz_j^*}{dt} = \frac{1}{2\pi} \left( \sum_{l \neq j}^N \Gamma_l \sum_{m=-\infty}^{\infty} \frac{\tilde{\chi}(z_j - z_l - 2Lm; \delta)}{z_j - z_l - 2Lm} - \sum_{l=1}^N \Gamma_l \sum_{m=-\infty}^{\infty} \frac{\tilde{\chi}(z_j - z_l^* - 2Lm; \delta)}{z_j - z_l^* - 2Lm} \right) + \partial_y \tilde{\phi} + i \partial_x \tilde{\phi},$$

where  $z_j = x_j + iy_j$ , the period in  $x$  is given by  $2L$ , and

$$\tilde{\chi}(r; \delta) = \left(1 - e^{-r^2/2\delta^2}\right) \left(1 + 2e^{-r^2/2\delta^2}\right).$$

We evaluate the corresponding sums over the image points  $z_j - z_l^*$  so as to keep the zero flow through  $z = 0$  condition strictly enforced.

Following the arguments in [4], and again emphasizing the compact support of the vorticity  $\omega(x, y, t)$ , we then have at the free surface the coupled nonlinear system

$$\partial_t \eta = -\partial_x \eta \partial_x \tilde{\phi} + \partial_z \tilde{\phi} + P_v,$$

and

$$\partial_t \tilde{\phi} + \frac{1}{2} |\nabla \tilde{\phi}|^2 + \text{Im} \{Q_v\} \partial_x \tilde{\phi} + \text{Re} \{Q_v\} \partial_z \tilde{\phi} + g\eta = E_v - \frac{1}{2} |Q_v|^2 + \frac{\sigma}{\rho_0} \partial_x \left( \frac{\partial_x \eta}{\sqrt{1 + (\partial_x \eta)^2}} \right)$$

where we have defined

$$c(\eta, z_j) = \cot \left( \frac{\pi}{2L} (\eta + H - z_j) \right),$$

so that

$$P_v = \text{Re} \{Q_v\} - \text{Im} \{Q_v\} \partial_x \eta,$$

$$Q_v = \frac{1}{4L} \sum_{j=1}^N \Gamma_j (c(\eta, z_j) - c(\eta, z_j^*)),$$

and

$$E_v = \frac{1}{4L} \sum_{j=1}^N \Gamma_j (\dot{x}_j \text{Im} \{c(\eta, z_j) - c(\eta, z_j^*)\} + \dot{y}_j \text{Re} \{c(\eta, z_j) + c(\eta, z_j^*)\})$$

Note, we have ignored the mollification given the separation between the surface and the point vortices used to approximate the vortex patch.

Defining  $q = \tilde{\phi}|_{z=\eta+H}$ , standard arguments [5, 4] allow for the derivation of series representations to the Dirichlet-to-Neumann operator  $G(\eta)$  so that

$$\eta_t = G(\eta)q + P_v,$$

and

$$\begin{aligned} \partial_t q + \frac{1}{2} (\partial_x q)^2 + g\eta - E_v + \frac{1}{2} |Q_v|^2 - \frac{\sigma}{\rho_0} \partial_x \left( \frac{\partial_x \eta}{\sqrt{1 + (\partial_x \eta)^2}} \right) = \\ - \frac{1}{1 + (\partial_x \eta)^2} \left( \left( P_v + \text{Re} \{Q_v\} - \frac{1}{2} (Gq + \partial_x \eta \partial_x q) \right) (Gq + \partial_x \eta \partial_x q) + \text{Im} \{Q_v\} (\partial_x q - \partial_x \eta Gq) \right) \end{aligned}$$

Thus, the surface boundary conditions can be recast entirely in terms of surface variables alone. This then leaves the problem of evaluating the derivatives of  $\tilde{\phi}$  at the vortex positions thereby allowing us to compute the speeds of the point vortices and closing the system of equations in terms of  $\eta$ ,  $q$ , and  $z_j$ . To do this, we repeat the arguments in [4], where it was shown that

$$\partial_y \tilde{\phi} + i \partial_x \tilde{\phi} \Big|_{z_j} = -\frac{1}{4L} \int_{-L}^L ((c(\eta, z_j) - c^*(\eta, z_j^*)) \partial_x q - i(c(\eta, z_j) + c^*(\eta, z_j^*)) G(\eta) q) dx$$

## Implementation Details for the Fast-Multipole Method

As can be seen, the presence of the mollifier prevents the closed form evaluation of the sums in  $m$ , thereby potentially adding significant overhead in numerical computations, even if fast Fourier transforms are used to evaluate the sums. We note however that

$$\tilde{\chi}(r; \delta) = 1 + \bar{\chi}(r), \quad \bar{\chi}(r) = \left(1 - 2e^{-r^2/2\delta^2}\right) e^{-r^2/2\delta^2}$$

which tacitly explains the role of mollification, which is to remove singularities in the determination of particle velocities when  $|z_j - z_l| \lesssim \delta$ . Thus, when we know that  $|z_j - z_l| > \delta$ , we take  $\tilde{\chi}(r; \delta) \sim 1$  so that

$$\frac{1}{2\pi} \sum_{m=-\infty}^{\infty} \frac{\tilde{\chi}(z_j - z_l - 2Lm; \delta)}{z_j - z_l - 2Lm} \approx \frac{1}{4L} \cot\left(\frac{\pi}{2L}(z_j - z_l)\right),$$

where the sum is taken in the principal value sense. In the case that  $|z_j - z_l| \lesssim \delta$ , we use instead

$$\frac{1}{2\pi} \sum_{m=-\infty}^{\infty} \frac{\tilde{\chi}(z_j - z_l - 2Lm; \delta)}{z_j - z_l - 2Lm} \approx \frac{1}{4L} \cot\left(\frac{\pi}{2L}(z_j - z_l)\right) + \frac{1}{2\pi} \frac{\bar{\chi}(z_j - z_l; \delta)}{z_j - z_l}.$$

The error incurred in these approximations is only exponentially small.

However, even in the best case scenario, the evaluation of the particle velocities is an  $\mathcal{O}(N^2)$  operation, and as we show later, we should anticipate there being large numbers of vortices in order to maintain the accuracy of our simulation. That being said, by employing a multi-level Barnes-Hut algorithm, which is an example of a Fast-Multipole Method (FMM), we can reduce the evaluation of the sums used to compute particle velocities to an  $\mathcal{O}(N \log N)$  operation. Further, our use of a FMM for the evaluation of the velocities  $\tilde{z}_j$  in effect determines all points either far or close to  $z_j$ , and thus it naturally selects when to use approximations appropriate for the cases  $|z_j - z_l| \leq \delta$  or  $|z_j - z_l| > \delta$ . The method relies crucially on the rapid convergence of the approximation

$$\cot(\tilde{z}_j - \tilde{z}_l) \approx \frac{(1 - \tan(\tilde{z}_j - c) \tan(c - \tilde{z}_l))}{\tan(\tilde{z}_j - c)} \sum_{m=0}^p (-1)^m \frac{\tan^l(c - \tilde{z}_l)}{\tan^l(\tilde{z}_j - c)},$$

where

$$\tilde{z} = \frac{\pi}{2L} z, \quad |\tilde{z}_l - c| < |\tilde{z}_j - c|.$$

Throughout the remainder of the simulations, we choose  $p = 10$ , which provides the necessary speed-up without sacrificing any significant accuracy in the computation of the point-vortex velocities.

## Shallow-Water Scalings and the KdV equation

So that we can work in a shallow-water environment, we introduce the scalings

$$\tilde{x} = \frac{x}{\lambda}, \quad \tilde{y} = \frac{y}{H}, \quad \tilde{t} = \frac{\sqrt{gH}}{L}t, \quad \eta = d\tilde{\eta}, \quad \tilde{\phi} = \mu L \sqrt{gH} \tilde{\tilde{\phi}}, \quad \tilde{\Gamma}_j = \frac{\Gamma_j}{\Gamma},$$

where we define the non-dimensional parameters

$$\mu = \frac{d}{H}, \quad \gamma = \frac{H}{\lambda}.$$

Note, in this scaling, we see that the vorticity  $\omega$  is then scaled as

$$\omega = \frac{\mu \sqrt{gH}}{H} \tilde{\omega},$$

so that by using Stoke's theorem, we see the net circulation  $\Gamma$  can be written as

$$\Gamma = \mu L \sqrt{gH} \tilde{\Gamma}, \quad \tilde{\Gamma} = \int_{\tilde{\Omega}} \tilde{\omega} d\tilde{A}.$$

Throughout the paper, we make reference to the nondimensional Froude number  $F$  to characterize the strength of the vortex patch. In these coordinates, it is given by

$$F = \frac{\Gamma}{\mu \lambda \sqrt{gH}}.$$

In the absence of vorticity, one can readily show that in the traveling coordinate  $\xi = x - t$  that the long time evolution of the tangential surface velocity  $Q = q_x$  and the surface  $\eta$  are found via the Korteweg–de Vries (KdV) equation,

$$2\partial_\tau Q + 3Q\partial_\xi Q + \frac{1}{3}\partial_\xi^3 Q = 0.$$

As is known, the KdV equation has an infinite number of periodic traveling wave solutions of the form

$$Q(x, t) \sim q_0 + 8\tilde{m}^2 \kappa^2 \text{cn}^2(\kappa(x - (1 + \mu\tilde{c})t); \tilde{m}), \quad (2)$$

where

$$\tilde{c} = \frac{2}{3}\kappa^2(2\tilde{m}^2 - 1) + \frac{3}{2}q_0,$$

and where  $0 \leq \tilde{m} < 1$  is the elliptic modulus of the cnoidal function  $\text{cn}(\cdot; \tilde{m})$  and where  $\mathcal{K}(\tilde{m})$  represents the complete elliptic integral of the first kind. This then implies that the surface profile is to leading order given by  $\eta \sim Q$ . We then choose initial conditions in our numerical simulations of free surface waves over vortex patches consistent with the traveling wave solutions of the KdV equation. Throughout the remainder of the paper,  $q_0 = 0$ .

## Implementation Details for the Lagrangian to Eulerian Regridding

As noted in [3] and examined in [2] and related papers, a major source of error in PVMs is the implicit grid distortion induced by the Lagrangian flow of the particles  $\mathbf{x}_j(t)$ . In particular, we can interpret the mollification parameter  $\delta$  as setting an effective radius of influence for each point  $\mathbf{x}_j(t)$ . The convergence theory associated with the PVM approximation, see [6], requires that if the particles  $\mathbf{x}_j$  start on a uniform mesh with mesh spacing  $h$ , then  $h < \delta$ , and this ‘overlapping’ must be maintained for all times of the simulation.

An especially effective means to ensure this was introduced in [7], where at some fixed number of time steps, the set of potentially irregular point positions and circulations, say

$$\{\mathbf{x}_j(t), \Gamma_j\}_{j=1}^N$$

are mapped onto a new, regularly  $h$ -spaced set of positions and corresponding circulations, say

$$\{\tilde{\mathbf{x}}_l, \tilde{\Gamma}_l\}_{l=1}^{\tilde{N}}.$$

This is done through the choice of a compactly supported interpolation kernel  $\Lambda(\cdot)$  so that

$$\tilde{\Gamma}_l = \sum_{j=1}^N \Gamma_j \Lambda\left(\frac{\tilde{x}_l - x_j}{h}\right) \Lambda\left(\frac{\tilde{y}_l - y_j}{h}\right).$$

As in [7], we choose the kernel  $\Lambda(x)$  so that

$$\Lambda(u) = \begin{cases} 1 - u^2, & 0 \leq |u| < \frac{1}{2} \\ \frac{1}{2}(1 - u)(2 - u), & \frac{1}{2} \leq |u| \leq \frac{3}{2} \\ 0, & |u| > \frac{3}{2} \end{cases}$$

This choice ensures that the net circulation and the associated first and second moments are preserved after regridding. It should be noted however that regridding in this way generically increases the total particle count so that  $\tilde{N} > N$ . This is largely due to having to add points  $\tilde{\mathbf{x}}_l$  relative to the distorted points  $\mathbf{x}_j$  furthest from the interior of the support of  $\omega(\mathbf{x}, t)$ .

We now model the initial vorticity via the circularly symmetric, compactly supported vorticity profile

$$\omega_0(r) = \begin{cases} \omega_m \left(1 - \frac{r^2}{R_v^2}\right)^3, & r \leq R_v \\ 0, & r > R_v \end{cases}$$

Given the circular symmetry of the profile, in the absence of a free surface or solid boundary, we know that  $\omega(\mathbf{x}, t) = \omega_0(r)$ . Using Equation (1) then, we can define a relative error  $\mathcal{E}(t)$  via the formula

$$\mathcal{E}(t) = \left( \frac{\sum_{l=1}^{\tilde{N}} |\omega_d(\tilde{\mathbf{x}}_l, t) - \omega(\tilde{\mathbf{x}}_l, t)|^2}{\sum_{l=1}^{\tilde{N}} |\omega(\tilde{\mathbf{x}}_l, t)|^2} \right)^{1/2}.$$

After introducing the shallow-water scalings described above, we choose  $\mu = .2$ ,  $\gamma = \sqrt{\mu}$ ,  $\omega_m = 1$ , and we run the simulations for  $0 \leq t \leq t_f = 10 = 2/\mu$ . Choosing a sampling rate of six time steps with  $dt = .05$  and  $\delta = 2h$ , we produce the following error profiles for  $h = .005$ ,  $.0067$ , and

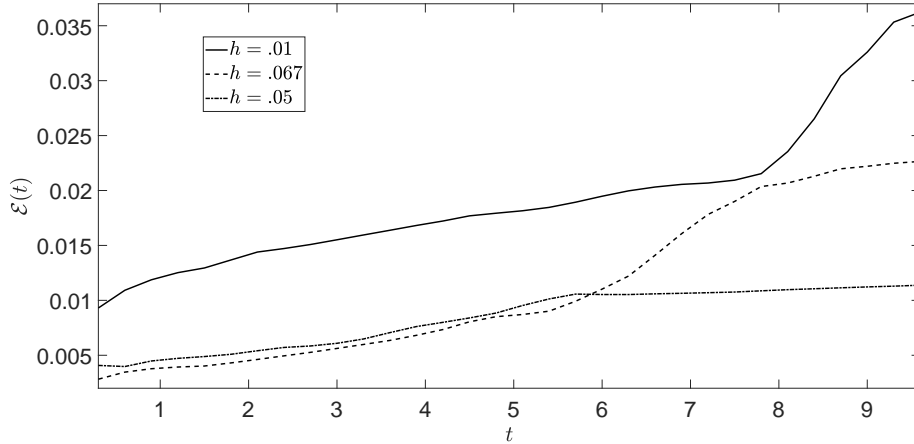


Figure 1: Error profiles for  $h = .005$ ,  $.0067$ , and  $.01$  with  $\delta = 2h$  and regridding done at every six time steps of the simulation.

$.01$  in Figure 1. As can be seen, while the overall error percentages are quite small in all cases, as one would expect, choosing  $h = .005$  and then maintaining that throughout the length of the simulation produces the most stable error profile.

However, the accuracy of the method must be contrasted against the computational expense incurred by introducing greater number of point-vortices at each regridding event. If we define  $N_s$  to be the initial number of point vortices and  $N_f$  to be the final number, we get the following table for differing values of  $h$  over the time interval  $0 \leq t \leq t_f$ .

$h$	$N_s$	$N_f$
$.005$	1252	11221
$.0067$	698	8385
$.01$	308	5937

Thus, throughout the remainder of the paper, we choose the middle path of  $h = .0067$ , which provides a relatively high-degree of accuracy while keeping the number of point vortices in the simulation at a more manageable level. Likewise, the increase in particle count and also position relative to the interior of the vorticity profile also raises the question of newly introduced points running into either the solid boundary at  $z = 0$  or the free surface at  $y = \epsilon\eta(x, t) + 1$ . We therefore modify the interpolation scheme so that vortices do not propagate past either  $z = 0$  or  $z = .9$ . Thus, while maintaining the accuracy of the PVM, this approach introduces significant overhead in the computation of particle velocities, which again is ameliorated through the use of a FMM.

## Results

Throughout this section, we take  $L = \lambda M$ , where  $M$  roughly counts the number of characteristic wavelengths included in the computational domain. Correspondingly, we take  $M = \mathcal{K}(\tilde{m})/\kappa$ , so that the period of the numerical simulation is equal to the period of the cnoidal wave. We note

that this does place some limits on the overall elliptic modulus we may pick since as  $\tilde{m} \rightarrow 1^-$ , the solitary wave limit moves the periodic copies of the vortices in the lateral direction off to infinity. This creates a series of source terms in the free boundary equations which decay only quadratically, thereby radically limiting the efficacy of a spectral method for modeling the surface. This is a fascinating complication beyond the scope of the present paper, but one that will be explored in future research.

With regards to the details of the simulations, we let  $\mu = .2$ ,  $\gamma = \sqrt{\mu}$ , which is consistent with the KdV approximation, and  $t_f = 2/\mu$ , so that nonlinearity has enough time to have a significant impact. Twenty terms are taken in the recursive computation of the DNO, and a total of  $K_T = 512$  modes are used for the pseudospectral approximation of the free surface. A Runge-Kutta 4 method with integrating factors is used with a time-step of  $\delta t = .05$ . We then have for our choice of vortex patch that  $F$  is given by

$$F = \frac{\pi\omega_0 R_v^2}{4\gamma}.$$

The radius of the patch,  $R_v$ , is chosen so that

$$R_v = \frac{\gamma}{2} \min\{1 - y_c, y_c\}$$

where  $y_c$  is the vertical displacement of the patch. We choose  $y_c = .35$ , so that  $R_v \approx .1565$ .

With these choices fixed, we note that the unscaled amplitude of the cnoidal wave initial conditions is given by  $8(\tilde{m}\kappa)^2$ . Throughout our simulations we have chosen  $\kappa$  for a given choice of elliptic modulus  $\tilde{m}$  so as to make this unscaled amplitude as close to unity as possible while still maintaining convergent numerical simulations. Note, this issue can of course be mollified by reducing the size of  $\mu$ , though this of course adds further choices in parameters, which are already numerous as is. In each of the following plots, we look at both the evolution of the vortex patch, and a comparison of the evolution of the free surface from the same initial conditions. Solid lines correspond to results in which  $\omega_0 \neq 0$  while dashed lines correspond to the zero vorticity case.

### Elliptic Modulus $\tilde{m} = .3$

Taking  $\tilde{m} = .3$  and  $\kappa = .5$ , this corresponds to  $M \approx 3.3$ . Taking  $K_T = 512$ , this gives  $\delta x = .013$ , thus making the surface wave mesh width almost ten times smaller than the radius of the vortex patch, thereby ensuring we can accurately capture surface oscillations on the scale of the patch. The unscaled amplitude of the cnoidal initial conditions is given by  $8(\tilde{m}\kappa)^2 \approx .18$ . As expected, stronger vorticity corresponds to greater deformation of the surface wave relative to the undisturbed case.

### Elliptic Modulus $\tilde{m} = .6$

Taking  $\tilde{m} = .6$ , we find that  $\kappa = .43$ , this corresponds to  $M \approx 4.4$ . Taking  $K_T = 512$ , this gives  $\delta x = .0172$ . The unscaled amplitude of the cnoidal initial conditions is given by  $8(\tilde{m}\kappa)^2 \approx .53$ . As seen in Figure 3, we see that the larger elliptic modulus and larger amplitude makes the surface wave less responsive to the impact of vorticity. Nevertheless, the patch consistently lowers maximum amplitudes, and when large enough, induces significant oscillations in the surface profile.

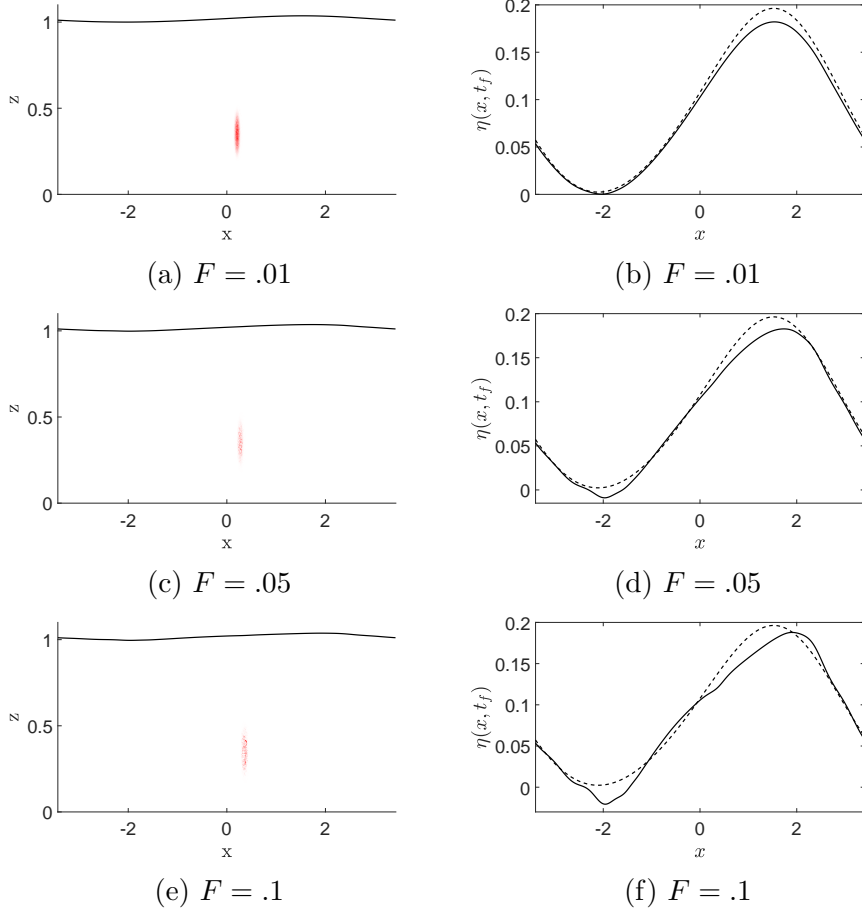


Figure 2: Waves over the vortex patch are shown on the left for various values of Froude number  $F$ , while comparisons of a cnoidal wave over a vortex patch(-) to a cnoidal wave over an irrotational fluid (-) are shown on the right. Here  $\mu = .2$ ,  $\gamma = \sqrt{\mu}$ ,  $t_f = 2/\mu$ ,  $\tilde{m} = .3$ ,  $\kappa = .5$ .



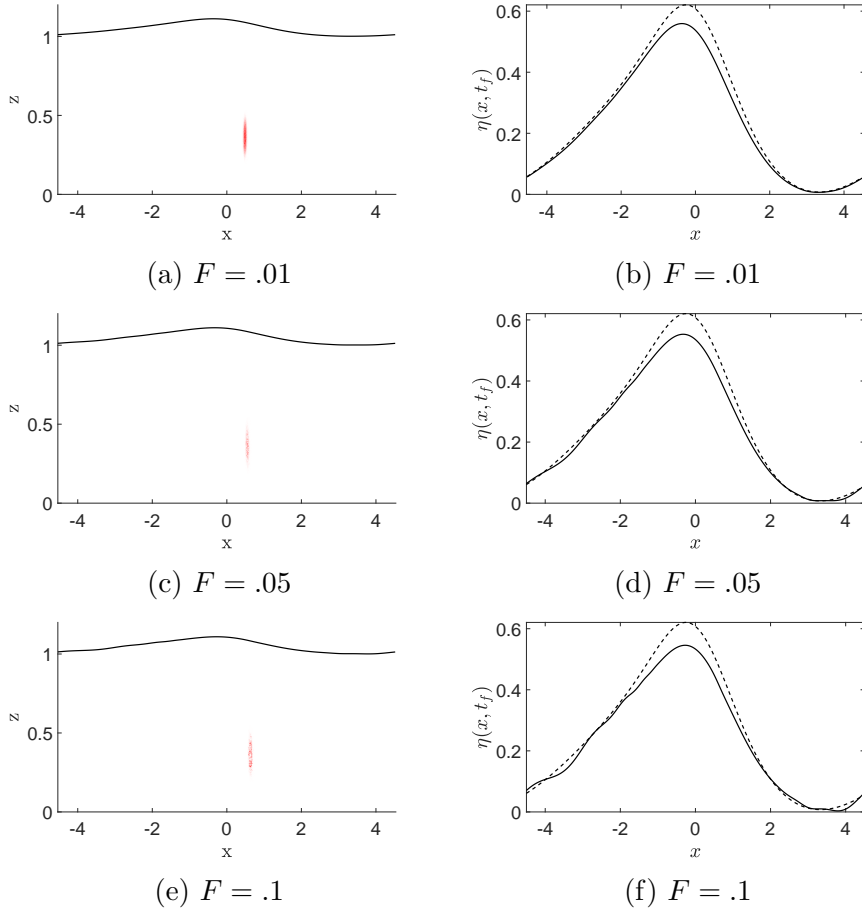


Figure 3: Waves over the vortex patch are shown on the left for various values of Froude number  $F$ , while comparisons of a cnoidal wave over a vortex patch(-) to a cnoidal wave over an irrotational fluid (-) are shown on the right. Here  $\mu = .2$ ,  $\gamma = \sqrt{\mu}$ ,  $t_f = 2/\mu$ ,  $\tilde{m} = .6$ ,  $\kappa = .43$ .

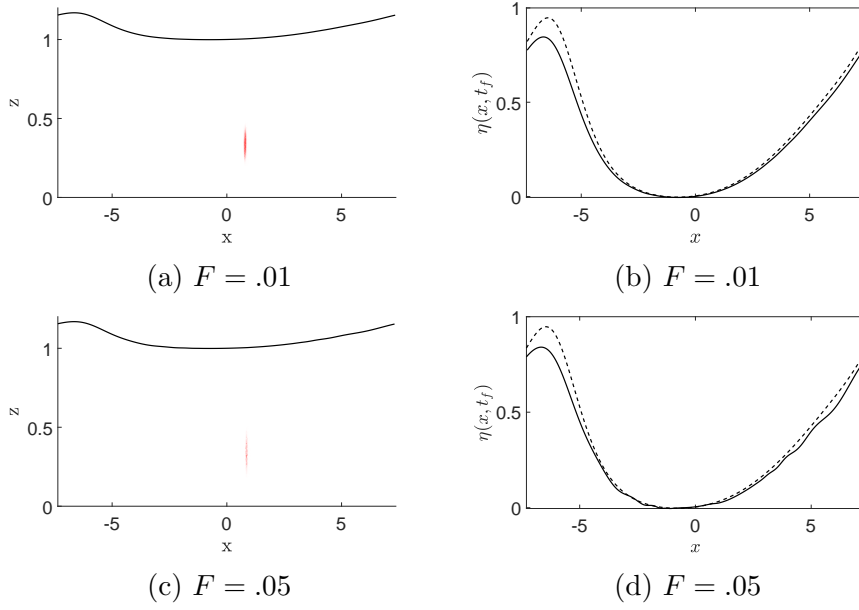


Figure 4: Waves over the vortex patch are shown on the left for various values of Froude number  $F$ , while comparisons of a cnoidal wave over a vortex patch(-) to a cnoidal wave over an irrotational fluid (-) are shown on the right. Here  $\mu = .2$ ,  $\gamma = \sqrt{\mu}$ ,  $t_f = 2/\mu$ ,  $\tilde{m} = .9$ ,  $\kappa = .35$ .

### Elliptic Modulus $\tilde{m} = .9$

Taking  $\tilde{m} = .9$ , we find that  $\kappa = .35$ , this corresponds to  $M \approx 7.4$ . Taking  $K_T = 512$ , this gives  $\delta x = .029$ . The unscaled amplitude of the cnoidal initial conditions is given by  $8(\tilde{m}\kappa)^2 \approx .8$ . Thus, somewhat suprisingly, we could use the largest amplitude wave when the initial condition was closest to that of a solitary wave profile. Likewise, aside from causing a slight broadening and thus decrease in maximum amplitude of the near solitary wave, vorticity has the least relative impact on the wave. Thus, if we treat the  $\tilde{m} = .9$  as the ‘most’ nonlinear of the three cases examined, since this corresponds to the case closest to that of a nonlinear solitary wave, we see vorticity has the least overall impact on the most nonlinear of waves.

With that being said, we were not able to get reliable results for vorticity strength  $\omega_0 = 10$ . In this case, a secondary vortex patch formed, which, on the face of it, is not possible in a smooth flow. Whether this is an artifact of underresolution, instability, or some other mechanism is not clear at this time and is the subject of future research.

## Conclusion

## Appendix

## References

- [1] P.G. Saffman. *Vortex Dynamics*. Cambridge University Press, Cambridge, 1992.

- [2] G.H. Cottet and P.D. Koumoutsakos. *Vortex Methods: Theory and Practice*. Cambridge University Press, Cambridge, 2000.
- [3] J.T. Beale and A. Majda. High order accurate vortex methods with explicit velocity kernels. *J. Comp. Phys.*, 58:188–208, 1985.
- [4] C.W. Curtis and H. Kalisch. Vortex dynamics in free-surface flows. *Phys. Fluids*, 29:032101, 2017.
- [5] W. Craig and C. Sulem. Numerical simulation of gravity waves. *J. Comput. Phys.*, 108:73–83, 1993.
- [6] G.H. Cottet. A new approach for the analysis of vortex methods in 2 and 3 dimensions. *Ann. Inst. Henri Poincaré*, 5:227–285, 1988.
- [7] P. Koumoutsakos and A. Leonard. High-resolution simulations of the flow around an impulsively started cylinder using vortex methods. *Jour. Fluid Mech.*, 296:1–38, 1995.